

Review

Active-Matrix Array Based on Thin-Film Transistors Using Emerging Materials for Application: From Lab to Industry

Seongjae Kim and Hocheon Yoo * 

Department of Electronic Engineering, Gachon University, Seongnam 13120, Republic of Korea

* Correspondence: hyoo@gachon.ac.kr

Abstract: The active-matrix technology incorporates a transistor to exert precise control over each pixel within a pixel array, eliminating the issue of crosstalk between neighboring pixels that is prevalent in the passive-matrix approach. Consequently, the active-matrix method facilitates the realization of high-resolution arrays, and this inherent advantage has propelled its widespread adoption, not only in display applications but also in diverse sensor arrays from lab to industry. In this comprehensive review, we delve into instances of active-matrix arrays utilizing thin-film transistors (TFTs) that leverage emerging materials such as organic semiconductors, metal oxide semiconductors, two-dimensional materials, and carbon nanotubes (CNTs). Our examination encompasses a broad classification of active-matrix research into two main categories: (i) displays and (ii) sensors. We not only assess the performance of TFTs based on emerging materials within the active-matrix framework, but also explore the evolving trends and directions in active-matrix-based displays and sensors.

Keywords: active-matrix; thin-film transistors; emerging materials; displays; sensors



Citation: Kim, S.; Yoo, H.

Active-Matrix Array Based on Thin-Film Transistors Using Emerging Materials for Application: From Lab to Industry. *Electronics* **2024**, *13*, 241. <https://doi.org/10.3390/electronics13010241>

Academic Editors: Elias Stathatos and Spyros N. Yannopoulos

Received: 4 December 2023

Revised: 24 December 2023

Accepted: 2 January 2024

Published: 4 January 2024



Copyright: © 2024 by the authors. Licensee MDPI, Basel, Switzerland. This article is an open access article distributed under the terms and conditions of the Creative Commons Attribution (CC BY) license (<https://creativecommons.org/licenses/by/4.0/>).

1. Introduction

Thin-film transistors (TFTs), based on field-effect transistors (FETs), are manufactured through a bottom-up process that involves the systematic stacking of layers. This bottom-up approach bestows significant process advantages, offering a considerable level of flexibility in structural design and material selection, thereby providing TFTs with a highly versatile platform. This design flexibility allows TFTs to extend beyond display backplanes [1–3] into various device areas, including digital and analog circuits [4–9] and image sensors [10–12]. In particular, many studies have been carried out recently to apply emerging materials such as organics [13–17], metal-oxide semiconductors [18–21], two-dimensional (2D) materials [22–24], and carbon nanotubes (CNTs) [25–28], rather than Si, as TFT channels.

While demonstrations have often been limited to the unit device level, proving practical device feasibility requires expanding to array scale. These array types are broadly categorized as passive-matrix [29,30] and active-matrix [31,32]. The passive-matrix takes the form of a crossbar array and has the advantage of a simple structure and low manufacturing cost. However, resolution improvement is constrained by crosstalk issues between adjacent pixels in the passive-matrix [32]. On the other hand, active-matrix, with a TFT in each pixel enabling independent pixel operation, avoids crosstalk and can achieve higher resolution [33]. This has led to the adoption of active-matrix not only in displays but also in various sensors, including photodetectors [34–36] and pressure sensors [37–39], etc.

In this review, we highlight research outcomes on active-matrix-based displays and various sensors, focusing particularly on studies implementing active-matrix with TFTs based on emerging materials. Furthermore, we revisit the specific purposes served by each sensor and explore the technologies they use. This review explains the interest of the use of the active-matrix approach across diverse applications and investigates its potential for expanding practicality from lab to industry.

2. Thin-Film Transistors and Active-Matrix Array

TFTs are mainly fabricated in a bottom-up process, unlike Si-based metal-oxide-semiconductor field-effect transistors (MOSFETs), which are manufactured in a top-down process [40]. A bottom-up process-based TFT is not only free in terms of designing device structure but also has excellent substrate compatibility [41–43]. In addition, a TFT can be implemented based on various processes such as spin coating [44,45], inkjet printing [46,47], photolithography [48,49], and thermal evaporation [50,51]. Through considerable effort, large-area processes have also become possible. Securing large-area process technology has enabled development beyond the characteristic evaluation at the unit device level to TFT-based system levels, such as digital and analog circuits, including active-matrix arrays. In particular, active matrices can be applied to various applications and offer many advantages. The active-matrix array is a method originally used for addressing the pixels in the display. Unlike the passive-matrix, which is a crossbar array that crosses horizontally and vertically, the active-matrix array contains one transistor per unit pixel. In the active-matrix, pixels are selected by controlling the on/off of the TFT. The very low off current of the TFT prevents the crosstalk issues that are problematic in the passive-matrix. This leads the active-matrix array to be used in various ways, such as sensor arrays and displays.

As mentioned earlier, the active-matrix array was initially adopted as an addressing method for displays and was later used to drive sensor arrays beyond displays. The driving methods of a sensor array and a display are not significantly different. A display converts electrical signals within the system into light. On the other hand, in a sensor array, the opposite process is achieved by converting information such as light and temperature into electrical signals through sensor devices and processing them in the internal system. In other words, both the display and the sensor array are the same up to the point of selecting a specific column through a switching transistor, and the only difference is the direction of signal transmission through the data line.

The implementation of an active-matrix array allows for the expression and sensing of more information, such as displaying a specific image or sensing the distribution of temperature or pressure. These unique features of the active-matrix array contribute to the ongoing development of advanced display and sensor systems.

3. Active-Matrix-Based Displays

3.1. Liquid Crystal Display (LCD)

A liquid crystal display (LCD) is one of the types of displays and is currently used in most televisions and monitors. The working principle is to control the amount of light transmitted by controlling the arrangement of liquid crystals located between two polarizers through voltage. To express color, color filters corresponding to red, green, and blue are used. Additionally, there are LCDs that are driven by using a reflector instead of a backlight to reflect external light. Cong et al. demonstrated an active-matrix polymer-dispersed liquid crystal (PDLC) seven-segment display using CNT TFT [52]. They utilized PDLC, formed by embedding micro-sized liquid crystals into a polymer matrix, and controlled the transparent or opaque state based on the refractive index difference between the polymer matrix and the liquid crystal, depending on the applied voltage (Figure 1a,b). The proposed PDLC display has a structure in which two ITO electrodes are sandwiched above and below the liquid crystal (Figure 1c). Figure 1d illustrates a CNT TFT-based backplane for driving a seven-segment display. The fabricated PDLC display demonstrated the ability to clearly distinguish light transmittance in the visible light region based on the voltage applied to both ends of the PDLC. Building on this capability, they successfully displayed numerical information by selectively controlling the liquid crystal of each pixel through CNT TFT.

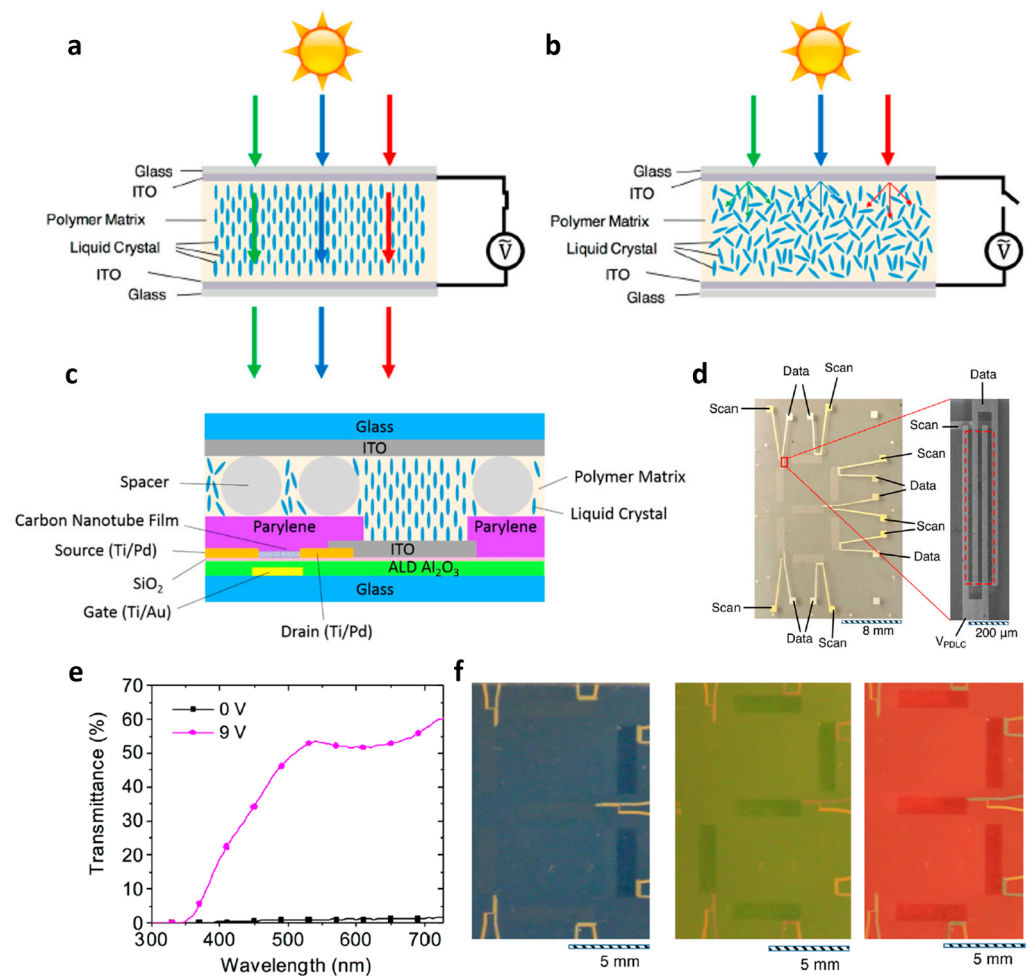


Figure 1. Active-matrix array-based liquid crystal display. (a) Transparent and (b) opaque states of PDLC pixels depending on whether or not voltage is applied to the electrode. (c) Cross-sectional view of a unit pixel of a PDLC display driven by CNT-TFT. (d) Optical image of the CNT-TFT-based back panel before PDLC integration and SEM image of the CNT-TFT. (e) Transmittance for wavelengths in transparent and opaque states depending on whether voltage is applied. (f) Demonstration of displaying the numbers “1”, “2”, and “3” on blue, green, and red backgrounds, respectively, by selectively making pixels transparent (adapted from [52] with permission from American Chemical Society).

3.2. Light-Emitting Diode (LED)

Unlike LCD, light-emitting diode does not require a backlight and the pixels emit light on their own; so, the pixels can be turned off completely, making real darkness possible. In addition, since there is no need for layers such as backlights and polarizers, as required in LCD, it is possible to implement thinner displays. These light-emitting diodes (LEDs) are divided into organic LED (OLED) [53–57], micro-LED (μ -LED) [58,59], and quantum dots LED (QLED) [60,61], depending on the materials used, and each is being actively researched and developed by several researchers. In particular, many attempts to apply emerging materials such as organic, oxide semiconductor, and 2D materials as backplanes have been reported.

Peng et al. developed a driving circuit for an 8×8 active-matrix LED based on organic TFTs (OTFTs) on paper [62]. They utilized paper with high roughness as a substrate, gradually alleviating the roughness by forming screen-printed silver and parylene-C as the gate electrode and gate dielectric. The reduced surface roughness led to the successful implementation of an 8×8 organic transistor array with a 100% yield (Figure 2a,b). Finally,

they integrated LEDs into the array and demonstrated the display of character information by controlling the active-matrix LEDs with the proposed organic transistor array (Figure 2c). This highlights the feasibility of implementing functional circuits, such as active-matrix arrays, using organic semiconductors even on rough substrates like paper.

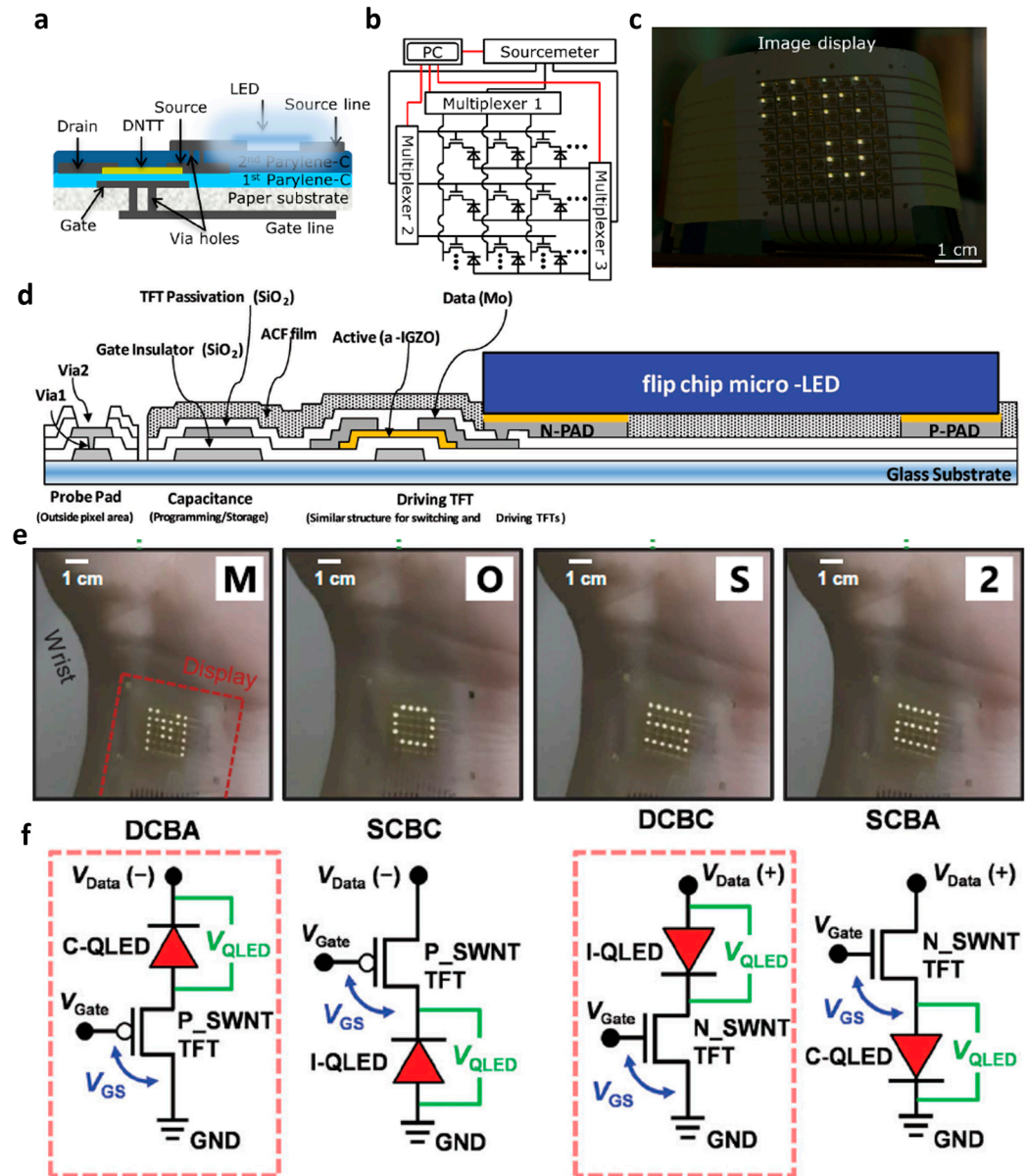


Figure 2. Active-matrix array-based light emitting diodes. (a) Cross-sectional view of a unit pixel of an OTFT-based active-matrix driver integrated with an LED. (b) Circuit scheme constructed to drive the array and (c) demonstration of display of text images (adapted from [62] with permission from Springer Nature). (d) Cross-sectional schematic diagram of a TFT- μ -LED pixel integrated through flip chip bonding (adapted from [63] with permission from John Wiley and Sons). (e) Driving a flexible OLED display based on a backplane circuit composed of MoS₂ attached to a human wrist (adapted from [64] with permission from American Association for the Advancement of Science). (f) Four different configurations to compare the characteristics of each combination of QLED structure and CNT TFT type (adapted from [65] with permission from John Wiley and Sons).

Um et al. developed an active-matrix LED display by integrating GaN μ -LEDs with an amorphous indium-gallium-zinc-oxide (a-IGZO) TFT backplane [63]. First, they fabricated the a-IGZO TFT backplane and GaN μ -LED pixel array on glass and sapphire substrates,

respectively. Subsequently, they completed the implementation of a 128×384 μ -LED array display by integrating the GaN μ -LED on the sapphire substrate into the a-IGZO TFT backplane through flip chip bonding (Figure 2d). The flip chip bonding process was conducted below 100 °C, ensuring no deterioration in the characteristics of the TFT backplane, and consequently, text and portrait images were successfully displayed on the display.

Choi et al. attempted to configure the backplane of the OLED display with MoS₂ TFT [64]. They optimized the characteristics of MoS₂ TFT before applying it as a driving TFT. The top and bottom of the MoS₂ channel were encapsulated with Al₂O₃, resulting in high on-current and low hysteresis characteristics. The introduction of the Al₂O₃ layer reduced the charge trap density at the interface, contributing to improved electrical properties. Using MoS₂ with enhanced characteristics, they implemented an OLED display on a flexible polymer substrate. The positive threshold voltage of the MoS₂ TFT reduced power consumption as it did not require a separate voltage to turn off the pixel. They demonstrated real-time control of text images by attaching a flexible OLED display with the manufactured MoS₂ backplane to a wrist (Figure 2e).

Baek et al. implemented a CNT TFT-based active-matrix QLED display [65]. In particular, to investigate the optimum design for a high-performance QLED array, they compared the characteristics of a total of four types of QLED arrays according to the type of driving TFT (*p*- or *n*-type) and the connection configuration between QLED and the driving transistor (conventional QLED or inverted QLED) (Figure 2f). They passivated Si₃N₄ on *p*-type CNT TFT to prepare *n*-type CNT TFT. The conversion of CNT TFT to *n*-type operation through Si₃N₄ passivation is because the positive fixed charge in Si₃N₄ causes *n*-type doping and protects it from atmospheric oxygen and water, which cause *p*-type doping effects [65,66]. Subsequently, the distinction between conventional QLED and inverted QLED was defined based on whether the upper Al and lower ITO electrodes served as cathode/anode or anode/cathode, respectively. At this point, depending on whether ITO, the bottom electrode of QLED, is in contact with the drain or source of the driving transistor, the cases were classified into four structures: (i) drain contact with the bottom anode (DCBA), (ii) source contact with the bottom cathode (SCBC), (iii) drain contact with the bottom cathode (DCBC), and (iv) source contact with the bottom anode (SCBA). As a result of comparing the electrical and optical characteristics of the four structures, when the QLED was connected to the source of the driving TFT (SCBC, SCBA), it showed poorer performance than when connected to the drain. This is because the voltage between the gate and source, which determines the drain current, is reduced due to the voltage drop occurring at the QLED. Therefore, when applying a *p*-type or *n*-type TFT as a driving TFT, it is advantageous to adopt the DCBA and DCBC structures. Based on this, they ultimately produced a 5×5 QLED array with *p*-type and *n*-type CNT TFTs as driving TFTs and demonstrated real-time display of character images.

3.3. Light-Emitting Electrochemical Cell (LEC)

Unlike OLED, which requires additional layers such as an electron injection layer and an electron transport layer in addition to the light-emitting layer, a light-emitting electrochemical cell (LEC) has a simple structure consisting of a light-emitting layer and two metal electrodes [67–70]. This simple structure is a great advantage, especially when implementing stretchable light-emitting devices. In order to provide elasticity to existing OLEDs, elasticity must be imparted to all layers, including the electron and hole injection layers as well as the light-emitting layer. However, in the case of LEC, only the light-emitting layer needs to be elastic; therefore, the process' difficulty is low.

Liu et al. utilized the advantages of LEC to implement an organic-based stretchable active-matrix organic LEC (OLEC) array [71]. They first fabricated a stretchable active-matrix TFT array to drive a stretchable OLEC array. They mixed a crosslinker containing flexible polydimethylsiloxane into conjugated polymers to prevent the semiconductor layer from delamination from the perfluorinated elastomer used as the gate dielectric when

the TFT is stretched (Figure 3a). At this time, the introduced crosslinker strengthened the bond between the two layers by crosslinking the conjugated polymers and the elastomeric dielectric layer during the annealing process, thereby preventing delamination of the semiconductor layer when stretching. Based on this, they successfully fabricated a stretchable TFT array (Figure 3b,c). Then, OLEC was integrated on the TFT array (Figure 3d), and it was demonstrated that OLEC could be driven through OTFT both without twisting and with twisting (Figure 3e,f).

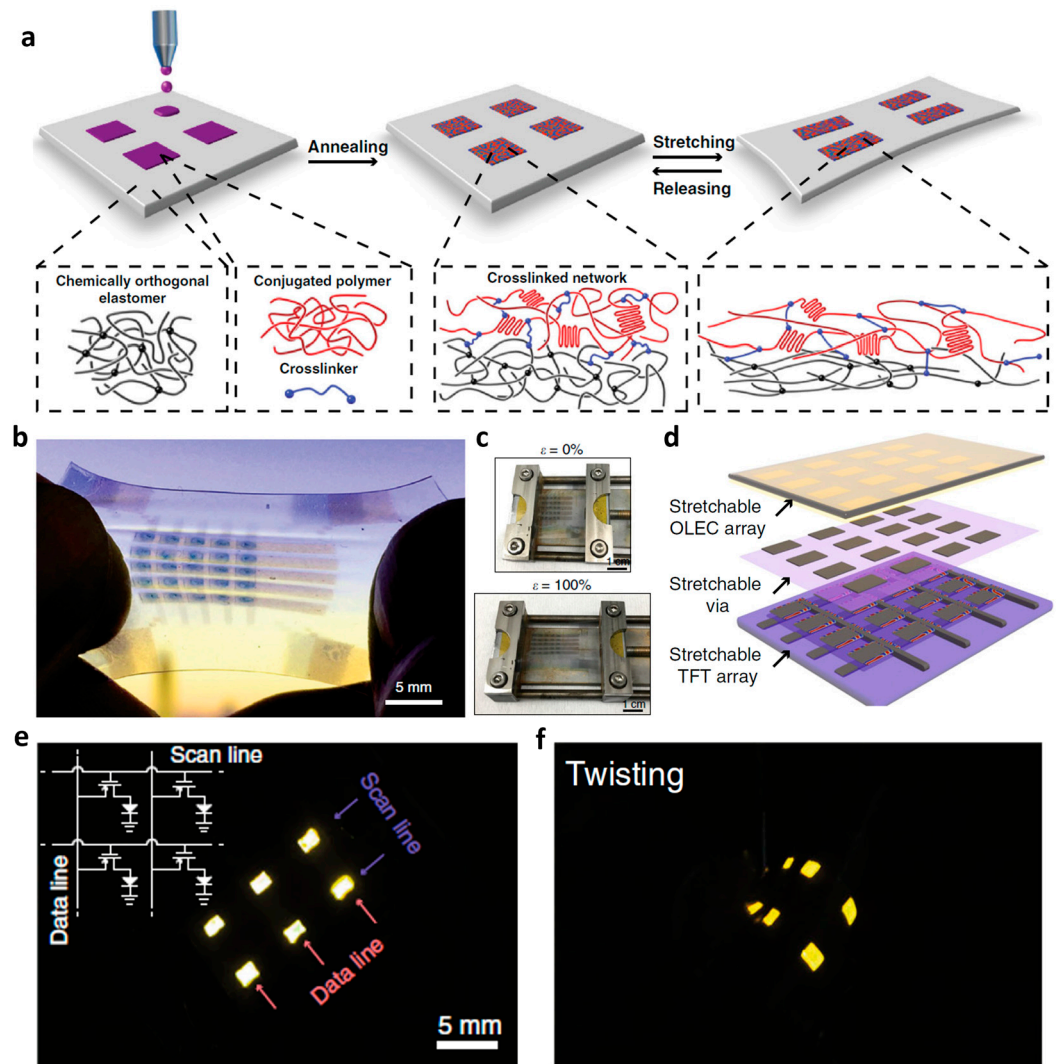


Figure 3. Active-matrix array-based light emitting electrochemical cell. (a) Cross-linking process with the dielectric layer through a cross-linker mixed in the semiconductor conjugated polymer to prevent the semiconductor layer from delamination the gate dielectric under stretching. (b) Photograph of a fully stretchable OTFT active-matrix array. (c) Strain testing from 0% to 100% of the stretchable transistor array. (d) Schematic diagram of vertical integration of active-matrix OTFT array and LEC array. Demonstration of operation of an active matrix OLEC array (e) with and (f) without twisting, respectively (adapted from [71] with permission from Springer Nature).

4. Active-Matrix-Based Sensors

Unlike displays that process internal electrical signals to output visual information, sensors play a crucial role by receiving information about specific external elements and converting it into corresponding electrical signals. Sensors are categorized based on the detection target, ranging from particles like photons [72–75] and gases [76–78] to external physical changes such as pressure [37,79,80], strain [81–83], and temperature [83,84]. The

development of these various sensors can provide many benefits to humans, such as preventing accidents from occurring caused by harmful elements such as toxic gases and ultraviolet, and enabling an accurate evaluation of the strength of products produced at manufacturing sites. Furthermore, by mimicking human sense organs such as vision and touch, sensors can contribute to the ongoing development of artificial intelligence and robotics, paving the way for innovative technologies in the future.

4.1. Photosensors

Photosensors are devices that convert optical signals into electrical signals and can perform the function of vision among the human senses. In addition, photosensors can be manufactured by targeting visible light [12,34,85], ultraviolet [86–88], and infrared [35,89,90] depending on the purpose. In particular, it is interesting that the presence or absence of light irradiation that humans cannot see, such as ultraviolet and infrared, can be detected through the photosensor.

Takahashi et al. achieved an imager capable of detecting visible light by monolithically integrating a CNT-based backplane with organic photodiodes [91]. They utilized PI substrates to take advantage of the material advantages of CNT, regioregular poly(3-hexylthiophene) (P3HT), and [6,6]-phenyl C61-butyric acid methyl ester (PCBM) in both TFTs and photodiodes. This approach resulted in the successful demonstration of a visible light imager with flexibility. Moreover, they integrated a Gd₂O₂S/Tb scintillator film, capable of converting X-rays into green light, into the visible light imager (Figure 4a,b). The introduction of the Gd₂O₂S/Tb scintillator film facilitated X-ray detection without causing damage to the organic active layer of the photodiode (Figure 4c).

X-rays possess strong energy and can be harmful to the human body, necessitating their detection for safety. In contrast, near-infrared (NIR), like X-rays, is invisible to humans but has very weak energy and is not harmful to the human body. Detection of NIR is significant as it can be utilized in various applications, including temperature measurement, near-field communication, and medical fields. In medical applications, the deep penetration characteristics of NIR enable measurements such as heart rate and oxygen saturation. Li et al. employed solution-processed In₂O₃ to construct the backplane of a NIR sensor array [89]. Additionally, they integrated solution-processed In₂O₃, known for its high electron mobility, into an NIR-responsive hybrid phototransistor along with an organic bulk heterojunction (Figure 4d). PTB7-Th and BTPV-4F were used as donor and acceptor materials, respectively, for the organic bulk heterojunction. Among the two materials, BTPV-4F is responsible for the actual absorption of NIR, while PTB7-Th is intended to improve the separation of electron–hole pairs through a built-in electric field generated by the formation of an organic bulk heterojunction. Finally, they manufactured a 16 × 16 hybrid NIR sensor array based on unit pixels in the form of one transistor–one phototransistor and successfully detected the NIR irradiation area.

The detection of a specific wavelength band, such as X-ray or NIR, is determined by the intended use of the sensor [92]. To imitate human vision, the sensor must be designed to target the visible light region, and each pixel should have the ability to distinguish between red, green, and blue light. Kim et al. introduced CdSe quantum dots as the active layer of a phototransistor on top of an a-IGZO transistor as a method to implement a color-selective imaging function. They initially demonstrated photodetector arrays with phototransistors capable of detecting red, green, and blue light, respectively, arranged in the lateral direction. Subsequently, to enhance the resolution, they attempted to vertically stack the quantum dots responsible for red, green, and blue. By investigating the photoresponse characteristics according to the stacking order of the red, green, and blue quantum dots, it was shown that stacking them from the bottom is the optimal structure. Based on this, they finally implemented color-selective photodetection at the same region by integrating an a-IGZO TFT-based backplane and a phototransistor with vertically stacked quantum dots.

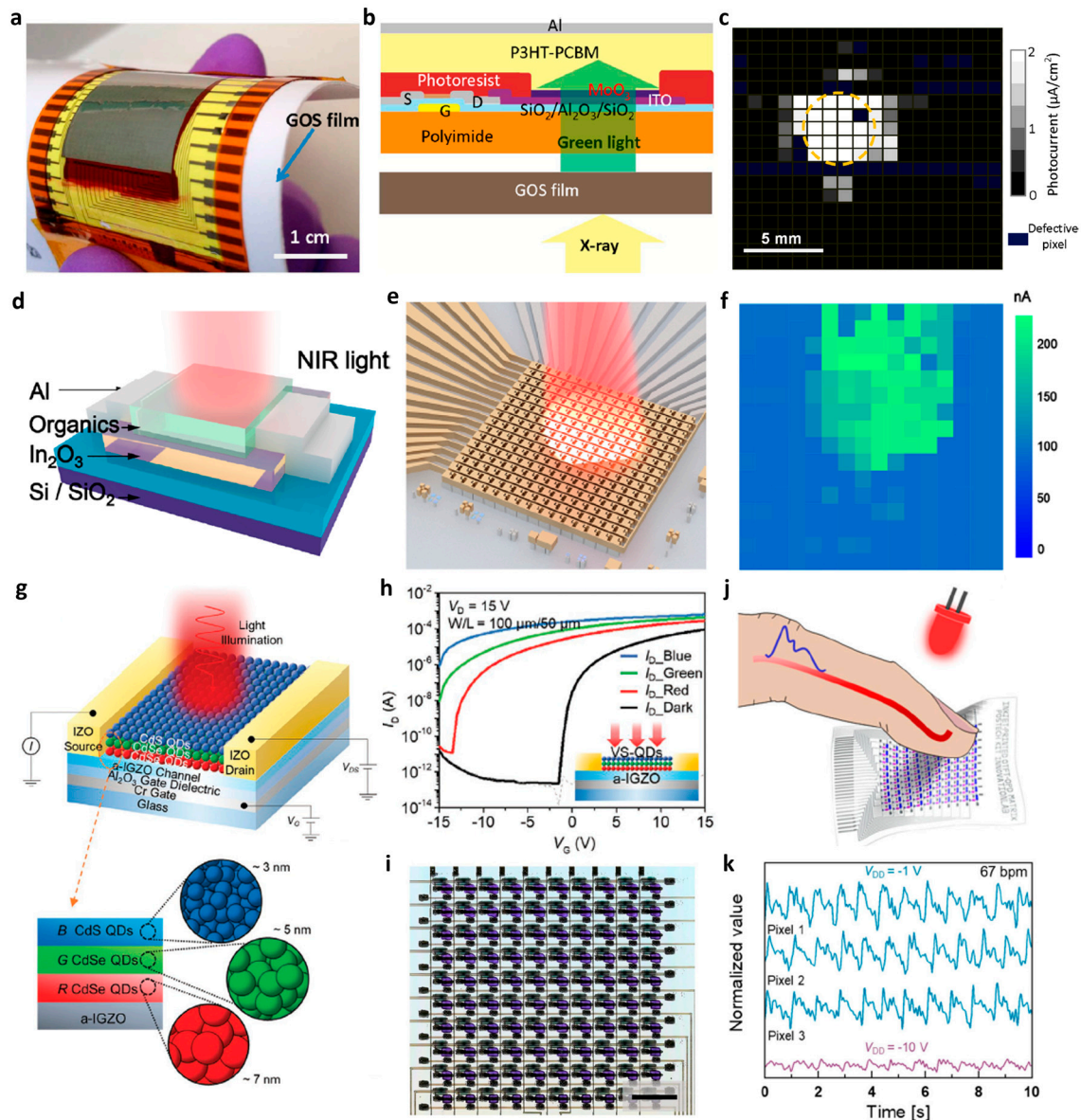


Figure 4. Active-matrix array-based photosensors. (a) Flexible imager integrated with a GOS film that converts X-rays into green light and (b) a cross-sectional view of one pixel. (c) Spatial mapping via an X-ray imager for irradiation of a circular X-ray source (adapted from [91] with permission from American Chemical Society). (d) Illustration of a hybrid phototransistor structure for NIR detection. (e) Scheme image in which the phototransistor array is irradiated with NIR and the corresponding (f) normalized photocurrent mapping of the phototransistor array (adapted from [89] with permission from American Chemical Society). (g) Schematic diagram of the structure of the vertically stacked QD/a-IGZO phototransistor and (h) transfer curve when irradiated with red, green, and blue light (adapted from [92] with permission from John Wiley and Sons). (i) A 10 × 10 active-matrix array based on an all-organic flexible photosensor, and (j) schematic of transmission mode-based PPG sensing and (k) measured pulse response (adapted from [93] with permission from Springer Nature).

The primary function of a photosensor is to detect light, but when its light-sensing properties are utilized, it can be actively employed in medical applications, such as for measuring a person's heart rate and oxygen saturation. Ruiz-Preciado et al. fabricated a highly flexible all-organic photosensor array by integrating organic photodiodes and OTFTs through an inkjet-printing process [93]. They demonstrated photoplethysmography (PPG) measurement by directing a red LED onto a finger and observing the pulsation.

ing blood flow through the current response in the photosensor array generated by the transmitted light.

4.2. Gas Sensor

Gas sensors are widely applied as devices that detect the presence of target gas in a specific space. In particular, measuring oxygen concentration or detecting harmful gases can inform people in the area of danger early and help them evacuate. Therefore, it is important for gas sensors to detect even minute levels of concentration quickly. Kim et al. demonstrated NO₂ gas detection using a two-step grown MoS₂ TFT-based gas sensor array (Figure 5a) [94]. Here, the two-step growing method proceeds with a sputtering step followed by a thermal sulfurization step. For both the switching TFT and the sensing TFT, two-step grown MoS₂ was applied as a channel, but the switching TFT was passivated with a SiO₂ layer to prevent reaction with gas (Figure 5b). In the case of the sensing TFT, the drain current decreased as the concentration of NO₂ gas increased (Figure 5c). This means that NO₂ gas increases the resistance of the MoS₂ channel, and when the concentration of each NO₂ gas was 128 ppm, the resistance increased by about 60% compared to the initial resistance (Figure 5d). The reason why MoS₂ TFT was able to react to NO₂ is because two-step grown MoS₂ has a poly-crystalline structure and many grain boundaries. In fact, for this reason, defects are intentionally formed to improve reactivity to gas.

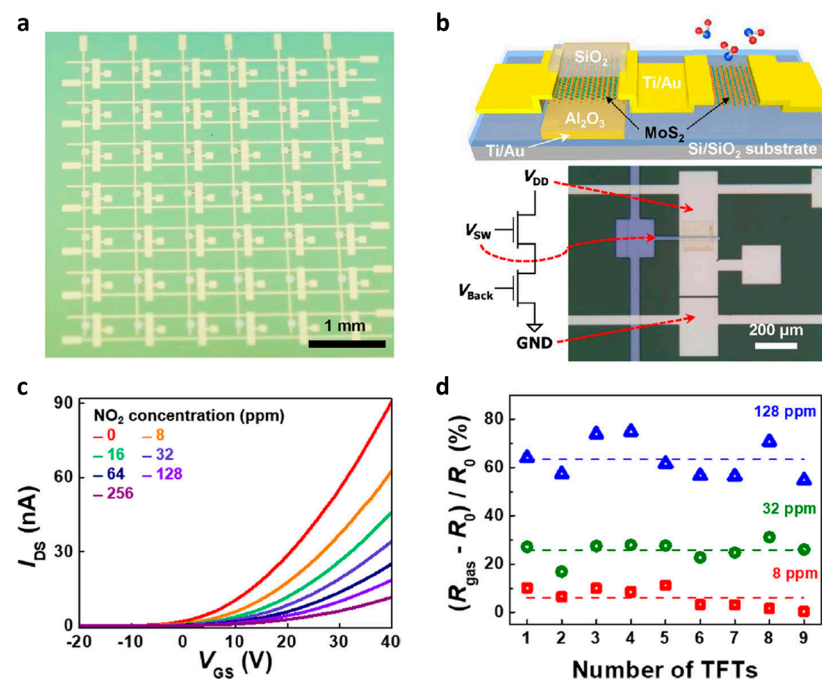


Figure 5. Active-matrix array-based gas sensor. (a) Image of MoS₂-based 7 × 6 active-matrix gas sensor, and (b) circuit schematic diagram and image consisting of switching TFT and sensing TFT. (c) Change in transfer curve of MoS₂ TFT according to NO₂ concentration. (d) Comparison of responses of nine MoS₂ gas sensors to the same NO₂ concentration (adapted from [94] with permission from Springer Nature).

Unlike photosensors and pressure sensors, gas sensors have not yet been implemented at the array level in many cases. This may be because, unlike other sensors that can obtain meaningful information by detecting specific image information or pressure distribution, gas sensors only need to detect the presence and concentration level of a specific gas. Therefore, if expanded in the direction of simultaneously detecting two or more different gases rather than just one specific gas, a gas sensor array could also be attractive.

4.3. Pressure Sensors

Shin et al. implemented a pressure sensor array based on graphene FET with air-dielectric [95]. They used two plastic panels connected by elastic joints as a substrate and created source/drain patterns and gate patterns on each panel. Afterward, by folding the elastic joint to the boundary, the two panels were completely overlapped and the FET structure was completed. At this time, the thickness of the air-dielectric corresponding to the gap between the graphene and the top gate is determined by the thickness of the elastomeric partition spacers. Therefore, the thickness of the air-dielectric and the pressure are inversely proportional, and as the pressure increases, the thickness of the gate dielectric of the graphene FET decreases. This means that an increase in pressure induces the capacitance of the gate dielectric, ultimately leading to an increase in the current of the graphene FET. Additionally, they successfully demonstrated a transparent pressure sensor array by introducing Ag NWs as electrodes (Figure 6a–c). However, the proposed graphene FET-based pressure sensor has limitations due to high off current; so, for low-power operation, the addition of FETs or other alternatives was needed to select each cell.

Jang et al. replaced graphene with MoS₂, a well-known 2D semiconductor, as the channel layer to address the high-off-current issue, a drawback in existing graphene FET-based pressure sensors [96]. Although MoS₂ has a two-dimensional structure, it differs from graphene in having a band gap suitable for a semiconductor channel. Notably, MoS₂ exhibits the ability to control electrical and optical properties depending on the number of layers. In the case of monolayer MoS₂, it possesses a direct band gap and outstanding optical properties. By incorporating monolayer MoS₂, which exhibits both excellent electrical and optical properties, into the pressure sensor, they successfully developed a pressure sensor array with low power consumption. Moreover, they leveraged the optical properties of monolayer MoS₂ to enhance pressure sensitivity further by introducing mechanoluminescent materials that emit visible light when compression or friction force is applied (Figure 6d). Through this approach, when pressure is applied to the MoS₂-based pressure sensor, not only does the dielectric thickness decrease, but the additional effect of excess carriers being created in MoS₂ by the emission of mechanoluminescent materials is introduced. This results in an increased amount of change in current for the same pressure (Figure 6e).

Among the existing pressure sensor types, in addition to the previously mentioned FET-type, many piezoresistive pressure sensors have been reported. The piezoresistive type offers the advantage of not only having a simple structure but also exhibiting high pressure sensitivity and enabling continuous sensing. Zhao et al. developed a pressure sensor utilizing a 64 × 64 CNT TFT-based backplane and a piezoresistive film (PRF) blended with CNT and thermoplastic polyurethane (TPU) elastomer (Figure 6f,g) [97]. Before the full-scale demonstration, they conducted a comprehensive investigation into the characteristics of the pressure sensor. The sensor demonstrated faster response times, with rising and falling times of 5 ms and 3 ms, respectively, compared to existing PRF-based pressure sensors. Additionally, the proposed pressure sensor exhibited excellent sensitivity and spatial resolution. Notably, it was demonstrated that the sensor could detect even the footprint of an artificial honeybee weighing 6.7 g, as illustrated in Figure 6h.

The high sensitivity of the pressure sensor allows it to detect even minute changes in pressure; so, it can also be applied to biosignal monitoring applications with weak signal strength. Karner-Petritz et al. implemented a pressure sensor array, utilizing a poly(vinylidene fluoride: trifluoroethylene) (P(VDF:TrFE))-based ferroelectric transducer and a DNNT-based OTFT for each pixel [98]. They fabricated an organic-based pressure sensor array on a 1 μm thick parylene substrate (Figure 6i). The ultra-flexible properties of the parylene substrate allow the pressure sensor array to be attached to uneven human skin. Exploiting this flexibility, they measured pulse waves using pressure sensors aligned with the direction of blood flow (Figure 6j). Moreover, they demonstrated the extraction of

pulse wave velocity and blood pressure by analyzing the time difference at the peak point of the pulse wave from sensors spaced apart from each other.

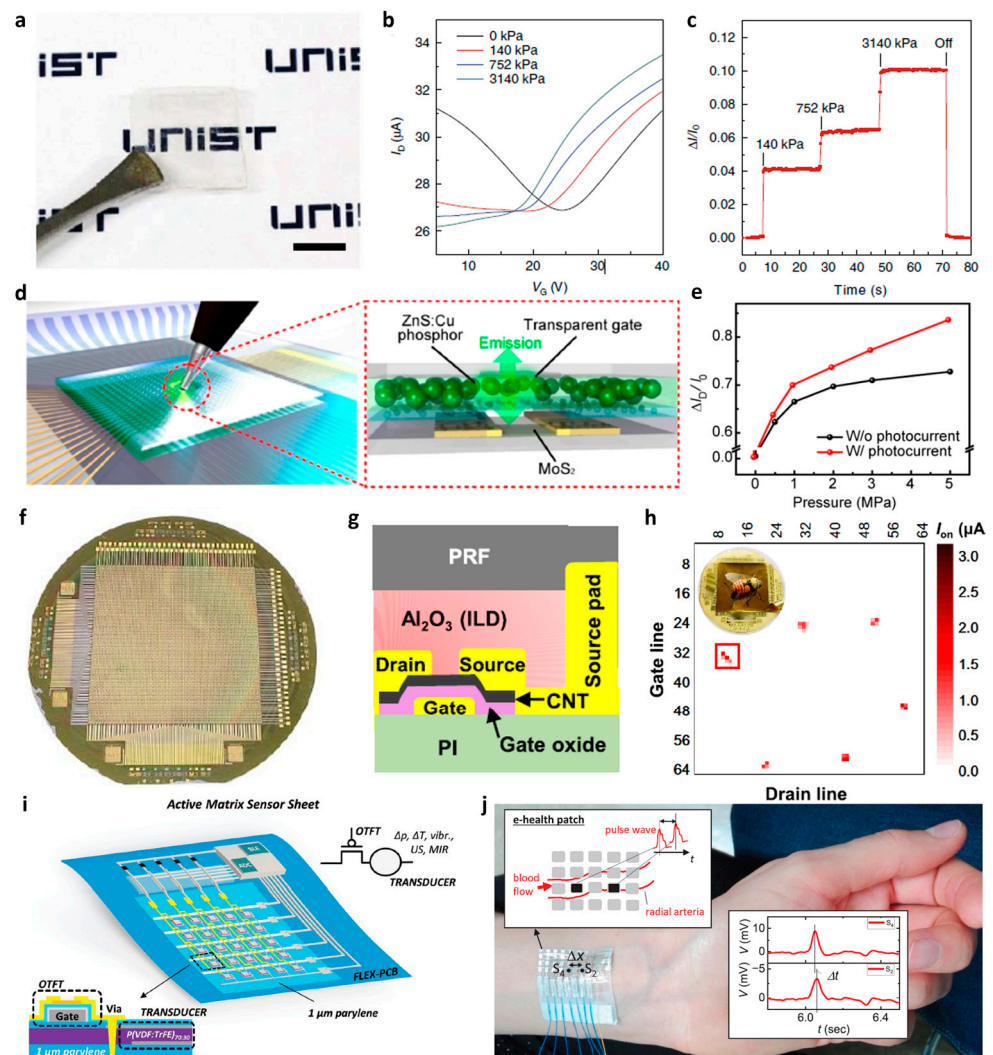


Figure 6. Active-matrix array-based pressure sensors. (a) Image of transparent pressure sensor based on air-dielectric graphene transistors. (b) Transfer curve of air-dielectric graphene transistors under various pressures and (c) measurement of change in drain current in response to real-time pressure change (adapted from [95] with permission from Springer Nature). (d) Illustration of MoS₂-based pressure sensor array with integrated phosphor particles with mechanoluminescence behavior. (e) Comparison of drain current change of MoS₂-based pressure sensor for pressure with and without phosphor particles (adapted from [96] with permission from American Chemical Society). (f) 64 × 64 active-matrix pressure sensor array composed of CNT TFTs and (g) cross-sectional schematic of unit pixels constituting the active-matrix pressure sensor array. (h) Current mapping through sensed pressure when an artificial bee is placed on a pressure sensor array (adapted from [97] with permission from American Chemical Society). (i) Schematic diagram of a pressure sensor array in which each pixel consists of a P(VDF:TrFE) ferroelectric transducer and DNNT OTFT. (j) Demonstration of pulse wave measurement by attaching a ferroelectric pressure sensor array to human skin (adapted from [98] with permission from John Wiley and Sons).

Efforts persist in enhancing the performance of diverse pressure sensors, with endeavors directed towards incorporating additional features, including transparency. The pursuit of high-performance pressure sensors holds significance as it can pave the way for the creation of bio-health devices characterized by low latency and high precision. Such

devices enable the monitoring of vital biological indicators like blood pressure and heart rate, contributing to advancements in healthcare technology.

4.4. Strain Sensors

Sun et al. fabricated an active-matrix strain sensor array by integrating a P(VDF-TrFE)-based piezoelectric nanogenerator (NG) and a graphene FET [99]. The bottom electrode of the piezoelectric NG and the gate electrode of the graphene FET are connected with patterned graphene (Figure 7a). Additionally, the conductivity of the graphene FET is determined by the potential of the graphene gate electrode through the electrolyte. As a result of evaluating the characteristics of the proposed strain sensor, they showed that when strain is applied to the device, the conductivity of the graphene FET is modulated as a piezoelectric potential is generated due to the alignment of the dipole in the PVDF that constitutes the piezoelectric NG. They further expanded the sensor to a 4×4 array based on piezopotential-gated graphene FETs and visualized the distribution of strain applied to the substrate.

In the context of strain sensors, being devices designed to measure externally applied stress, they operate in an environment where the components can be susceptible to damage through repetitive measurements. Consequently, there is a need for research aimed at enhancing the reliability of strain sensors to facilitate continuous sensing. Oh et al. introduced a semiconductor thin film with self-healing properties, offering insights into addressing reliability issues in strain sensors [100]. They employed a semiconductor thin film comprising a mixture of DPP-TVT-PDCA and PDMS-PDCA-Fe elastomer, determining through an examination of carrier mobility at various mixing ratios that the optimal ratio was 1:5. The self-healing properties of the proposed semiconductor thin film mixed with DPP-TVT-PDCA and PDMS-PDCA-Fe elastomer result from the presence of abundant dynamic metal–ligand coordination bonds [101]. Finally, they fabricated a 5×5 strain sensor array and performed additional passivation to prevent device malfunction due to human sweat, showing that the electrical characteristics remained stable even after 15 h after dropping artificial sweat on the sensor array. After verifying the stability aspects, including the self-healing properties, they successfully visualized the distribution of strain by mapping the current of the sensors that make up the array when the center of the 5×5 strain sensor array was pierced with a plastic tip (Figure 7c–e).

As mentioned earlier, in order to improve the reliability and durability of the strain sensor, it is necessary to not only ensure stability to the semiconductor layer but also consider the stress in the interconnection between the components that make up the device. Li et al. investigated the stress distribution throughout the strain sensor through simulation when a horizontally increasing strain was applied to a resistive strain sensor consisting of an elastic sensitive region and two electrodes at both ends (Figure 7f) [102]. A noticeable stress peak occurred at the interface between the elastic-sensitive region and the electrode, which means that in the strain sensor of the aforementioned structure, the junction between the electrode and the elastic-sensitive region is an unstable element with a high possibility of malfunction. Hence, they introduced an additional interconnected layer to mitigate stress at the contact area while preserving the strain sensing characteristics. Consequently, it was confirmed that the peak stress in the strain sensor was reduced by more than threefold (Figure 7g). Based on this, they introduced a CB-PDMS/Ecoflex interconnected layer into a strain sensor with Ag NW embedded in PDMS elastomer and Ag paste as the sensitive region and electrode, respectively, and secured stability at the contact area. Finally, by integrating a strain sensor into the flexible active-matrix OLED display, they could sense the distribution of strain according to the bending of the display and through this, implemented an interactive surface (Figure 7h).

Zhao et al. developed a multi-modal sensor capable of simultaneously detecting both strain and relative humidity [103]. They applied and integrated graphene and MoS₂ to sense strain and relative humidity, respectively. Even though the two sensing functions were performed simultaneously, mutual interference was avoided because graphene was

insensitive to humidity and, conversely, MoS₂ had a negligible response to humidity. They attached the proposed multimodal sensor to a mask to measure human breathing frequency, conducting measurements both before and after exercise. During this process, they could extract the breathing frequency by analyzing the cycle in which the peak of resistance changes for the measured strain and humidity occurred. Additionally, it was possible to observe changes in humidity attributed to exhalation. Consequently, while enhancing the performance of sensors such as sensitivity and response time is crucial, expanding the capability to sense multiple elements within the same area represents a direction for further advancement in the sensor field.

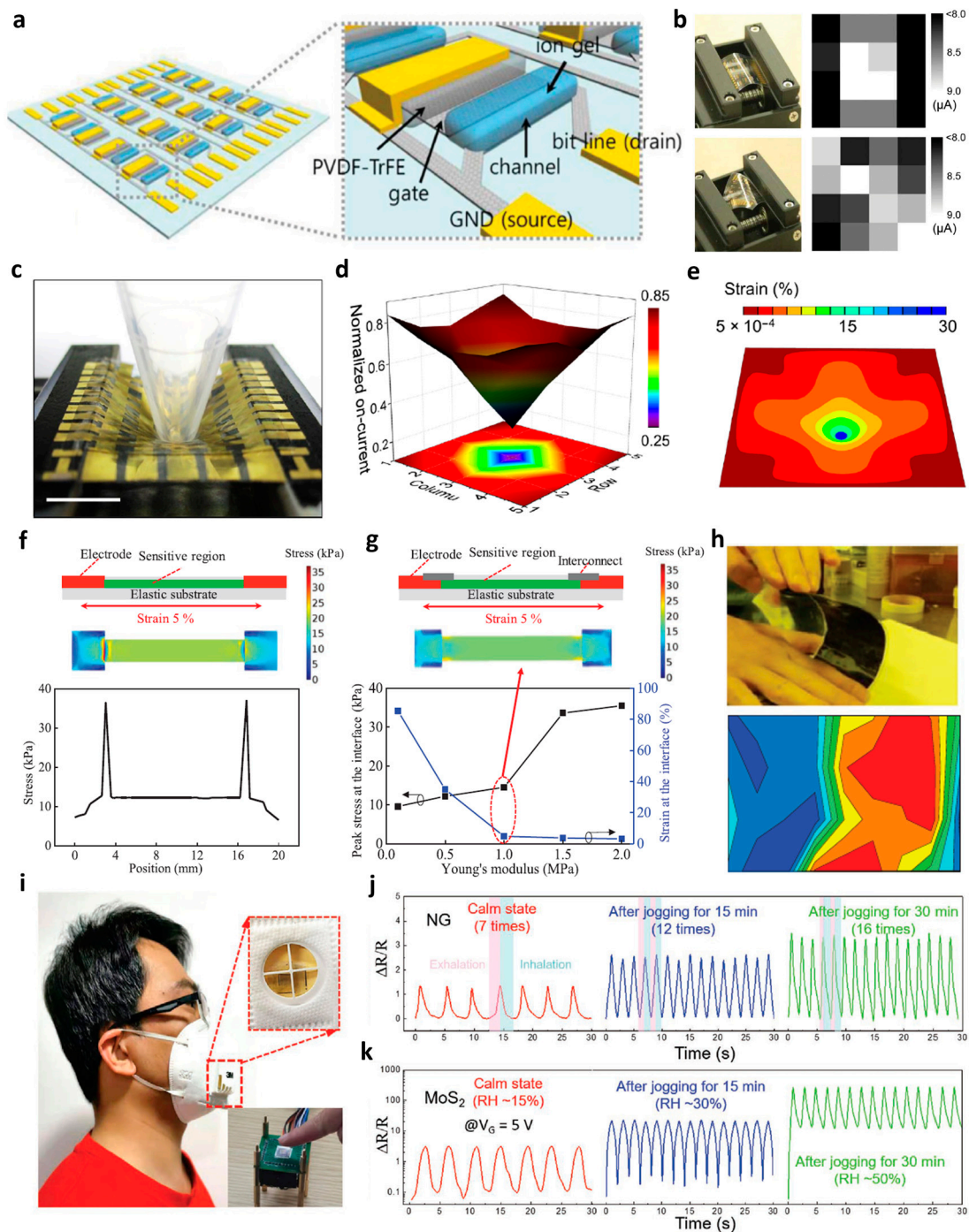


Figure 7. Active-matrix array-based strain sensors. (a) Structural schematic diagram of an active-matrix strain sensor array based on a piezopotential-gated graphene transistor. (b) 2D mapping of

the output current of each pixel comprising the strain sensor array when an external strain is applied (adapted from [99] with permission from John Wiley and Sons). (c) A photograph of a self-healable semiconducting polymer-based active-matrix strain sensor being poked with a plastic tip to evaluate its properties, and (d) the normalized on current of the strain sensor array at that time and (e) strain mapping obtained through simulation (adapted from [100] with permission from American Association for the Advancement of Science). When applying a horizontally increasing strain to a resistive strain sensor consisting of an elastic sensitive region and two electrodes at either end, stress distribution in the sensor region (f) with and (g) without an interconnection layer. (h) Mapping of strain distribution through resistance change according to bending operation after integrating the strain sensor with the display (adapted from [102] with permission from John Wiley and Sons). (i) A photo showing the insertion of a sensor capable of simultaneously measuring strain and humidity into a mask to monitor human breathing frequency, intensity, and RH. Changes in resistance over time of (j) strain-sensitive graphene and (k) humidity-sensitive MoS₂ caused by human respiration before and after exercise (adapted from [103] with permission from John Wiley and Sons).

4.5. Temperature Sensors

Hong et al. constructed a temperature sensor array based on a CNT TFT backplane [104]. The temperature sensor array consists of a total of four layers, excluding Ecoflex, which is used as a flexible substrate. The CNT TFT and temperature sensor are positioned on the first and fourth layers, respectively, starting from the bottom (Figure 8a). The gate and source lines for array configuration are located on the second and third layers. Notably, the gate and source lines are constructed using Galinstan, ensuring that the electrical characteristics remain stable even when the Ecoflex board is deformed. Moreover, electrochemically synthesized polyaniline nanofiber film was employed as the temperature sensor channel and had a resistance sensitivity of 1.0% °C⁻¹ in the range from 15 to 45 °C (Figure 8b). Subsequently, following the integration of the temperature sensor with the CNT TFT, a linear change in current corresponding to temperature was observed (Figure 8c). This enabled the calculation of the temperature based on the change in drain current when a finger contacted the 5 × 5 temperature sensor array. Remarkably, the calculated temperature value closely matched the measurement obtained with an infrared thermometer.

Ren et al. implemented a temperature sensor array consisting of a DNNT TFT and a pentacene/Ag NPs thermistor in a 16 × 16 array (Figure 8d) [105]. The constructed temperature sensor array demonstrated the ability to detect temperatures in the range of 20 to 100 °C, achieving a temperature resolution of 0.4 °C. In the case of the DNNT TFT, the change in electrical characteristics in the relevant temperature range was negligible. Instead, only the resistance of the pentacene/Ag NPs thermistor exhibited a sensitive response to temperature. To validate the practicality of the temperature sensor, they placed a 2 cm × 2 cm Peltier heater on the sensor, inducing a temperature change. They successfully performed 2D temperature mapping using the temperature sensor array (Figure 8e). Moreover, by utilizing the flexible properties of poly(ethylene naphthalate) (PEN) used as a substrate, they demonstrated the measurement of body temperature by attaching the sensor to a person's forehead.

The two previous temperature sensor arrays were implemented by integrating a thermistor with a resistance change sensitive to temperature on a TFT-based backplane that is insensitive to temperature change. In addition, the focus was on implementing a temperature sensor and demonstrating the measurement of the temperature distribution of an object or body temperature. Furthermore, Kim et al. proposed a flexible temperature sensor array designed for low-power operation [106]. To achieve a temperature sensor capable of low-power operation, they used a voltage range corresponding to the subthreshold region of the transistor because the subthreshold region is located near 0 V, which naturally leads to low power consumption. In addition, the characteristic that transport of carriers in the subthreshold region is mainly achieved by temperature-sensitive diffusion could serve as an opportunity to sense temperature at the subthreshold region. The implemented

subthreshold transistor-based temperature sensor operated stably even under strain of up to 100%, and its sensitivity to temperature was recorded at a very high $9.4\% \text{ } ^\circ\text{C}^{-1}$. Additionally, they successfully measured the surface temperature of a cold or hot spherical metal ball using the proposed temperature sensor (Figure 8f–h).

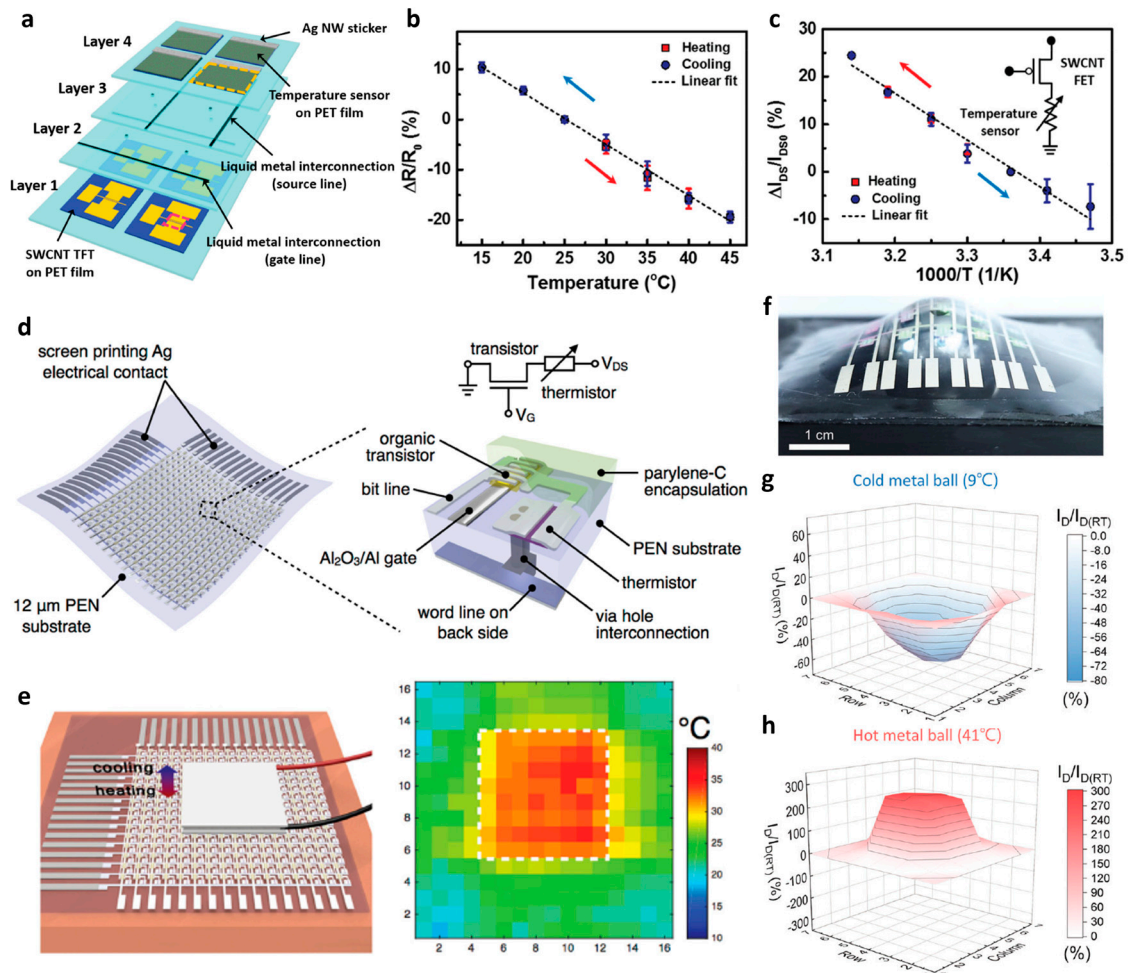


Figure 8. Active-matrix array-based temperature sensors. (a) Schematic diagram of a polyaniline nanofiber temperature sensor array with CNT TFT backplane consisting of a total of four layers. (b) Change in the normalized resistance of polyaniline nanofiber-based temperature sensor according to temperature. (c) Change in the normalized drain current of the sensor after integration of the CNT TFT and temperature sensor (adapted from [104] with permission from John Wiley and Sons). (d) Circuit diagram and device structure of the unit temperature sensor constituting the flexible temperature sensor array. (e) Schematic diagram of heated temperature distribution measurement and 2D temperature mapping via Peltier heater located on top of the temperature sensor array (adapted from [105] with permission from John Wiley and Sons). (f) Scheme image of measuring the surface temperature of a metal ball using a stretchable temperature sensor array. Three-dimensional mapping through the distribution of normalized drain current extracted from the temperature sensor when the metal ball is (g) cold and (h) hot, respectively (adapted from [106] with permission from John Wiley and Sons).

5. Summary

In this review, we reported on studies that implemented an active-matrix array using TFTs based on emerging materials such as organic semiconductors, metal oxide semiconductors, 2D materials, and CNTs (Tables 1 and 2). The versatility of the TFT-based active-matrix, which can overcome resolution limitations due to crosstalk issues in the

passive-matrix, became the reason for introducing the active-matrix not only in displays but also in various sensors. In addition, TFTs based on the bottom-up process offer a high degree of design flexibility, allowing for freedom in material and structure selection during production. The freedom of choice regarding design parameters allows TFTs to be manufactured not only on rigid substrates such as silicon and glass, but also on flexible substrates based on paper and polymers. As a result, many attempts have been reported to provide flexibility and stretchability to active-matrix-based displays and various sensors. In particular, the flexible and stretchable sensor array produced allows for close contact with surfaces that are not flat, such as human skin. This is used in healthcare to measure biological signals by minimizing the gap between the sensor and the surface to which it is attached. It enables precise measurements in the monitoring system.

Table 1. Previous research on active-matrix array-based displays.

Application	Transistor Materials	Emission Materials	Wavelength Band	Quantum Efficiency	Array Scale	Ref.
LCD	CNT	-	-	-	5 × 5	[52]
micro-LED	DNTT	micro-LED module	White	-	8 × 8	[62]
micro-LED	a-IGZO	GaN	456 nm	-	384 × 128	[63]
OLED	MoS ₂	Alq ₃ /C ₅₄₅ T	-	-	6 × 6	[64]
QDLED	CNT	CdSe/Cd _x Zn _{1-x} Se/ZnS QDs	609 nm	19.1%	5 × 5	[65]
OLEC	PII2T	SY/ionic elastomer	-	-	5 × 5	[71]

Table 2. Previous research on various sensor arrays based on active-matrix.

Sensor Type	Transistor Materials	Sensor Materials	Sensitivity	Operating Voltage	Array Scale	Ref.
Photo	CNT	P3HT:PCBM	0.15 AW ⁻¹	5 V	18 × 18	[91]
Photo	In ₂ O ₃	PTB7-Th/BTPV-4F	1393 AW ⁻¹	10 V	16 × 16	[89]
Photo	a-IGZO	CdS QD, CdSe QD	5.2 × 10 ³ AW ⁻¹	15 V	12 × 12	[92]
Photo	DPP-DTT	P3HT-IDTBR	0.356 AW ⁻¹	10 V	10 × 10	[93]
Gas	MoS ₂	MoS ₂	-	10 V	7 × 6	[94]
Pressure	Graphene	Graphene	2.05 × 10 ⁻⁴ kPa ⁻¹	30 V	12 × 12	[95]
Pressure	MoS ₂	MoS ₂	0.045 Mpa ⁻¹	60 V	20 × 20	[96]
Pressure	CNT	MWCNTs/TPU composite	385 kPa ⁻¹	3 V	64 × 64	[97]
Pressure	DNTT	P(VDF:TrFE)	0.12 nC N ⁻¹	3 V	12 × 12	[98]
Strain	Graphene	P(VDF:TrFE)	Gauge factor (GF): 69	1 V	4 × 4	[99]
Strain	DPP-PDCA-PDMS	DPP-PDCA-PDMS	GF: 5.75 × 10 ⁵	60 V	5 × 5	[100]
Strain	-	AgNWs	-	-	4 × 9	[102]
Strain	MoS ₂	Graphene	GF: 412	5 V	10 × 10	[103]
Temperature	CNT	polyaniline nanofiber	1.0% °C ⁻¹	10 V	5 × 5	[104]
Temperature	a-IGZO	Mxene	-	4 V	16 × 16	[105]
Temperature	DPPT-TT	DPPT-TT	9% °C ⁻¹	1 V	5 × 5	[106]

There are many advantages to active-matrix using emerging-material-based TFTs, and the following matters need to be considered for further development to reach industrialization in the future. (i) Although it is important to improve the performance of TFTs based on emerging materials integrated into the active-matrix, it is necessary to secure reliability through continuous research and evaluation of operation stability that can maintain stable characteristics in various surrounding environments. (ii) In the case of active-matrix sensors, development is needed to detect two or more factors within the same area. This will be important in the development of gas sensors capable of detecting and identifying multiple gases, especially in the field of gas sensors that are less scalable to array scale. (iii) In addition, in order to advance to the industrialization stage, technology for manufacturing a high-resolution active-matrix array must be secured through improvements in the fine process level to improve the integration of TFTs based on emerging materials. As has been the case so far, the development of emerging-material-based TFT and active-matrix-based displays and sensors will continue to be implemented by many researchers, and it is clear that it will have a beneficial impact on our lives in the future.

Author Contributions: S.K. performed literature research, analysis, and wrote the paper. H.Y. initiated and supervised the work and wrote the paper. All authors have read and agreed to the published version of the manuscript.

Funding: This research was partly supported by the Technology Innovation Program (1415181712, Interface Technology of 3D Stacked Heterogeneous System for SCM-based Process-in-Memory) funded by the Ministry of Trade, Industry & Energy (MOTIE, Korea). This work was supported in part by the Gachon University Research Fund of 2023 (GCU-202307950001).

Conflicts of Interest: The authors declare no conflicts of interest.

References

1. Zhu, H.; Shin, E.S.; Liu, A.; Ji, D.; Xu, Y.; Noh, Y.Y. Printable semiconductors for backplane TFTs of flexible OLED displays. *Adv. Funct. Mater.* **2020**, *30*, 1904588. [[CrossRef](#)]
2. Wu, W.-J.; Chen, J.-W.; Wang, J.-S.; Zhou, L.; Tao, H.; Zou, J.-H.; Xu, M.; Wang, L.; Peng, J.-B.; Chan, M. High-resolution flexible AMOLED display integrating gate driver by metal–oxide TFTs. *IEEE Electron Device Lett.* **2018**, *39*, 1660–1663. [[CrossRef](#)]
3. Meng, W.; Xu, F.; Yu, Z.; Tao, T.; Shao, L.; Liu, L.; Li, T.; Wen, K.; Wang, J.; He, L. Three-dimensional monolithic micro-LED display driven by atomically thin transistor matrix. *Nat. Nanotechnol.* **2021**, *16*, 1231–1236. [[CrossRef](#)] [[PubMed](#)]
4. Lei, T.; Shao, L.-L.; Zheng, Y.-Q.; Pitner, G.; Fang, G.; Zhu, C.; Li, S.; Beausoleil, R.; Wong, H.-S.P.; Huang, T.-C. Low-voltage high-performance flexible digital and analog circuits based on ultrahigh-purity semiconducting carbon nanotubes. *Nat. Commun.* **2019**, *10*, 2161. [[CrossRef](#)] [[PubMed](#)]
5. Janneck, R.; Nowack, T.S.; De Roose, F.; Ali, H.; Dehaene, W.; Heremans, P.; Genoe, J.; Rolin, C. Integration of highly crystalline C8-BTBT thin-films into simple logic gates and circuits. *Org. Electron.* **2019**, *67*, 64–71. [[CrossRef](#)]
6. Andersson Ersman, P.; Lassnig, R.; Strandberg, J.; Tu, D.; Keshmiri, V.; Forchheimer, R.; Fabiano, S.; Gustafsson, G.; Berggren, M. All-printed large-scale integrated circuits based on organic electrochemical transistors. *Nat. Commun.* **2019**, *10*, 5053. [[CrossRef](#)] [[PubMed](#)]
7. Shim, J.; woon Jang, S.; Lim, J.-H.; Kim, H.; Kang, D.-H.; Kim, K.-H.; Seo, S.; Heo, K.; Shin, C.; Yu, H.-Y. Polarity control in a single transition metal dichalcogenide (TMD) transistor for homogeneous complementary logic circuits. *Nanoscale* **2019**, *11*, 12871–12877. [[CrossRef](#)] [[PubMed](#)]
8. Polyushkin, D.K.; Wachter, S.; Mennel, L.; Paur, M.; Paliy, M.; Iannaccone, G.; Fiori, G.; Neumaier, D.; Canto, B.; Mueller, T. Analogue two-dimensional semiconductor electronics. *Nat. Electron.* **2020**, *3*, 486–491. [[CrossRef](#)]
9. Lu, W.; Lu, C.; Yang, G.; Liu, M.; Chen, K.; Liao, F.; Duan, X.; Lu, N.; Li, L. Monolithically Stacked Two Layers of a-IGZO-Based Transistors Upon a-IGZO-Based Analog/Logic Circuits. *IEEE Trans. Electron Devices* **2023**, *70*, 1697–1701. [[CrossRef](#)]
10. Xu, Y.; Ruan, C.-P.; Zhou, L.; Zou, J.-H.; Xu, M.; Wu, W.-J.; Wang, L.; Peng, J.-B. A 256 × 256, 50- μm pixel pitch OPD image sensor based on an IZO TFT backplane. *IEEE Sens. J.* **2021**, *21*, 20824–20832. [[CrossRef](#)]
11. Yokota, T.; Fukuda, K.; Someya, T. Recent progress of flexible image sensors for biomedical applications. *Adv. Mater.* **2021**, *33*, 2004416. [[CrossRef](#)] [[PubMed](#)]
12. Chen, T.; Wang, C.; Yang, G.; Lou, Q.; Lin, Q.; Zhang, S.; Zhou, H. Monolithic Integration of Perovskite Photoabsorbers with IGZO Thin-Film Transistor Backplane for Phototransistor-Based Image Sensor. *Adv. Mater. Technol.* **2023**, *8*, 2200679. [[CrossRef](#)]
13. Luo, Z.; Peng, B.; Zeng, J.; Yu, Z.; Zhao, Y.; Xie, J.; Lan, R.; Ma, Z.; Pan, L.; Cao, K. Sub-thermionic, ultra-high-gain organic transistors and circuits. *Nat. Commun.* **2021**, *12*, 1928. [[CrossRef](#)] [[PubMed](#)]
14. Casula, G.; Lai, S.; Martino, L.; Santoro, F.; Bonfiglio, A.; Cosseddu, P. Printed, low-voltage, all-organic transistors and complementary circuits on paper substrate. *Adv. Electron. Mater.* **2020**, *6*, 1901027. [[CrossRef](#)]
15. Jiang, C.; Choi, H.W.; Cheng, X.; Ma, H.; Hasko, D.; Nathan, A. Printed subthreshold organic transistors operating at high gain and ultralow power. *Science* **2019**, *363*, 719–723. [[CrossRef](#)] [[PubMed](#)]
16. Shin, H.-S.; Yoo, H.; Kim, C.-H. Revealing Three-in-One Nature of Organic Negative Transconductance Transistors. *IEEE Trans. Electron Devices* **2022**, *69*, 5149–5154. [[CrossRef](#)]
17. Kim, C.-H. Contact resistance in organic transistors: Use it or remove it. *Appl. Phys. Rev.* **2020**, *7*, 031306. [[CrossRef](#)]
18. Carlos, E.; Leppäniemi, J.; Sneek, A.; Alastalo, A.; Deuermeier, J.; Branquinho, R.; Martins, R.; Fortunato, E. Printed, highly stable metal oxide thin-film transistors with ultra-thin high- κ oxide dielectric. *Adv. Electron. Mater.* **2020**, *6*, 1901071. [[CrossRef](#)]
19. Zhao, Y.; Wang, Z.; Xu, G.; Cai, L.; Han, T.H.; Zhang, A.; Wu, Q.; Wang, R.; Huang, T.; Cheng, P. High Performance Indium-Gallium-Zinc Oxide Thin Film Transistor via Interface Engineering. *Adv. Funct. Mater.* **2020**, *30*, 2003285. [[CrossRef](#)]
20. Bukke, R.N.; Mude, N.N.; Saha, J.K.; Jang, J. High performance of a-IZTO TFT by purification of the semiconductor oxide precursor. *Adv. Mater. Interfaces* **2019**, *6*, 1900277. [[CrossRef](#)]
21. Li, G.; Wu, Y.; Li, Y.; Hong, Y.; Zhao, X.; Reyes, P.I.; Lu, Y. Early stage detection of Staphylococcus epidermidis biofilm formation using MgZnO dual-gate TFT biosensor. *Biosens. Bioelectron.* **2020**, *151*, 111993. [[CrossRef](#)]
22. Das, S.; Sebastian, A.; Pop, E.; McClellan, C.J.; Franklin, A.D.; Grasser, T.; Knobloch, T.; Illarionov, Y.; Penumatcha, A.V.; Appenzeller, J. Transistors based on two-dimensional materials for future integrated circuits. *Nat. Electron.* **2021**, *4*, 786–799. [[CrossRef](#)]

23. Daus, A.; Vaziri, S.; Chen, V.; K roglu,  .; Grady, R.W.; Bailey, C.S.; Lee, H.R.; Schauble, K.; Brenner, K.; Pop, E. High-performance flexible nanoscale transistors based on transition metal dichalcogenides. *Nat. Electron.* **2021**, *4*, 495–501. [[CrossRef](#)]
24. Wang, Z.; Wang, P.; Wang, F.; Ye, J.; He, T.; Wu, F.; Peng, M.; Wu, P.; Chen, Y.; Zhong, F. A noble metal dichalcogenide for high-performance field-effect transistors and broadband photodetectors. *Adv. Funct. Mater.* **2020**, *30*, 1907945. [[CrossRef](#)]
25. Liu, L.; Han, J.; Xu, L.; Zhou, J.; Zhao, C.; Ding, S.; Shi, H.; Xiao, M.; Ding, L.; Ma, Z. Aligned, high-density semiconducting carbon nanotube arrays for high-performance electronics. *Science* **2020**, *368*, 850–856. [[CrossRef](#)] [[PubMed](#)]
26. Lin, Y.; Liang, S.; Xu, L.; Liu, L.; Hu, Q.; Fan, C.; Liu, Y.; Han, J.; Zhang, Z.; Peng, L.M. Enhancement-Mode Field-Effect Transistors and High-Speed Integrated Circuits Based on Aligned Carbon Nanotube Films. *Adv. Funct. Mater.* **2022**, *32*, 2104539. [[CrossRef](#)]
27. Xu, L.; Qiu, C.; Peng, L.-m.; Zhang, Z. Suppression of leakage current in carbon nanotube field-effect transistors. *Nano Res.* **2021**, *14*, 976–981. [[CrossRef](#)]
28. Pitner, G.; Zhang, Z.; Lin, Q.; Su, S.-K.; Gilardi, C.; Kuo, C.; Kashyap, H.; Weiss, T.; Yu, Z.; Chao, T.-A. Sub-0.5 nm interfacial dielectric enables superior electrostatics: 65 mV/dec top-gated carbon nanotube FETs at 15 nm gate length. In Proceedings of the 2020 IEEE International Electron Devices Meeting (IEDM), San Francisco, CA, USA, 12–18 December 2020; pp. 3.5.1–3.5.4.
29. Bornemann, S.; G link, J.; Moro, V.; Gil, J.C.; Wolter, S.; Sch ttler, G.; Bezshlyakh, D.; Prades, J.D.; Dieguez, A.; Waag, A. Processing and characterization of monolithic passive-matrix GaN-based microLED arrays with pixel sizes from 5 to 50  m. *IEEE Photonics J.* **2021**, *13*, 1–9. [[CrossRef](#)]
30. Nau, S.; Wolf, C.; Sax, S.; List-Kratochvil, E.J. Organic Non-Volatile Resistive Photo-Switches for Flexible Image Detector Arrays. *Adv. Mater.* **2015**, *27*, 1048–1052. [[CrossRef](#)]
31. Choi, M.; Jang, B.; Lee, W.; Lee, S.; Kim, T.W.; Lee, H.J.; Kim, J.H.; Ahn, J.H. Stretchable active matrix inorganic light-emitting diode display enabled by overlay-aligned roll-transfer printing. *Adv. Funct. Mater.* **2017**, *27*, 1606005. [[CrossRef](#)]
32. Park, Y.J.; Sharma, B.K.; Shinde, S.M.; Kim, M.-S.; Jang, B.; Kim, J.-H.; Ahn, J.-H. All MoS₂-based large area, skin-attachable active-matrix tactile sensor. *ACS Nano* **2019**, *13*, 3023–3030. [[CrossRef](#)] [[PubMed](#)]
33. Jang, J.; Oh, B.; Jo, S.; Park, S.; An, H.S.; Lee, S.; Cheong, W.H.; Yoo, S.; Park, J.U. Human-interactive, active-matrix displays for visualization of tactile pressures. *Adv. Mater. Technol.* **2019**, *4*, 1900082. [[CrossRef](#)]
34. Liu, C.; Zhou, H.; Wu, Q.; Dai, F.; Lau, T.K.; Lu, X.; Yang, T.; Wang, Z.; Liu, X.; Liu, C. Guided Formation of Large Crystals of Organic and Perovskite Semiconductors by an Ultrasonicated Dispenser and Their Application as the Active Matrix of Photodetectors. *ACS Appl. Mater. Interfaces* **2018**, *10*, 39921–39932. [[CrossRef](#)] [[PubMed](#)]
35. Wang, Y.; Chen, C.; Zou, T.; Yan, L.; Liu, C.; Du, X.; Zhang, S.; Zhou, H. Spin-On-Patterning of Sn–Pb Perovskite Photodiodes on IGZO Transistor Arrays for Fast Active-Matrix Near-Infrared Imaging. *Adv. Mater. Technol.* **2019**, *5*, 1900752. [[CrossRef](#)]
36. Xuan, Y.; Lu, Y.; Honda, S.; Arie, T.; Akita, S.; Takei, K. Active-Matrix-Based Flexible Optical Image Sensor. *Adv. Mater. Technol.* **2021**, *6*, 2100259. [[CrossRef](#)]
37. Ji, S.; Jang, J.; Hwang, J.C.; Lee, Y.; Lee, J.H.; Park, J.U. Amorphous Oxide Semiconductor Transistors with Air Dielectrics for Transparent and Wearable Pressure Sensor Arrays. *Adv. Mater. Technol.* **2019**, *5*, 1900928. [[CrossRef](#)]
38. Baek, S.; Lee, Y.; Baek, J.; Kwon, J.; Kim, S.; Lee, S.; Strunk, K.P.; Stehlin, S.; Melzer, C.; Park, S.M.; et al. Spatiotemporal Measurement of Arterial Pulse Waves Enabled by Wearable Active-Matrix Pressure Sensor Arrays. *ACS Nano* **2022**, *16*, 368–377. [[CrossRef](#)] [[PubMed](#)]
39. Ma, C.; Xu, D.; Wang, P.; Lin, Z.; Zhou, J.; Jia, C.; Huang, J.; Li, S.; Huang, Y.; Duan, X. Two-dimensional van der Waals thin film transistors as active matrix for spatially resolved pressure sensing. *Nano Res.* **2021**, *14*, 3395–3401. [[CrossRef](#)]
40. Rustagi, S.; Singh, N.; Fang, W.; Buddhharaju, K.; Omampuliyur, S.; Teo, S.; Tung, C.; Lo, G.; Balasubramanian, N.; Kwong, D. CMOS inverter based on gate-all-around silicon-nanowire MOSFETs fabricated using top-down approach. *IEEE Electron Device Lett.* **2007**, *28*, 1021–1024. [[CrossRef](#)]
41. Singh, S. Fully solution-processed carbon nanotubes thin film transistors and PMOS inverters on glass substrate. *Flexible and Printed Electronics* **2023**, *8*, 015011. [[CrossRef](#)]
42. Bhalerao, S.R.; Lupo, D.; Berger, P.R. Flexible, solution-processed, indium oxide (In₂O₃) thin film transistors (TFT) and circuits for internet-of-things (IoT). *Mater. Sci. Semicond. Process.* **2022**, *139*, 106354. [[CrossRef](#)]
43. Li, X.; Ren, Y.; Wang, X.; Shao, S.; Li, H.; Wu, L.; Liu, X.; Zhao, J. A universal method for high-efficiency immobilization of semiconducting carbon nanotubes toward fully printed paper-based electronics. *Adv. Electron. Mater.* **2021**, *7*, 2001025. [[CrossRef](#)]
44. Chen, D.; Xu, Y.; An, Z.; Li, Z.; Zhang, C. Thin-film transistors based on wide bandgap Ga₂O₃ films grown by aqueous-solution spin-coating method. *Micro Nano Lett.* **2019**, *14*, 1052–1055. [[CrossRef](#)]
45. Ruzgar, S.; Caglar, M. The effect of Sn on electrical performance of zinc oxide based thin film transistor. *J. Mater. Sci. Mater. Electron.* **2019**, *30*, 485–490. [[CrossRef](#)]
46. Shao, F.; Wan, Q. Recent progress on jet printing of oxide-based thin film transistors. *J. Phys. D Appl. Phys.* **2019**, *52*, 143002. [[CrossRef](#)]
47. Singh, S.; Takeda, Y.; Matsui, H.; Tokito, S. Flexible PMOS inverter and NOR gate using inkjet-printed dual-gate organic thin film transistors. *IEEE Electron Device Lett.* **2020**, *41*, 409–412. [[CrossRef](#)]
48. Zschieschang, U.; Klauk, H.; Borchert, J.W. High-Resolution Lithography for High-Frequency Organic Thin-Film Transistors. *Adv. Mater. Technol.* **2023**, *8*, 2201888. [[CrossRef](#)]
49. Cui, N.; Ren, H.; Tang, Q.; Zhao, X.; Tong, Y.; Hu, W.; Liu, Y. Fully transparent conformal organic thin-film transistor array and its application as LED front driving. *Nanoscale* **2018**, *10*, 3613–3620. [[CrossRef](#)] [[PubMed](#)]

50. Kim, S.; Seo, J.; Park, T.; Yoo, H. Interface Trap-Free, 100% Yield, Wafer-Scale, Non-Volatile Optically-Guided Memory Array from Cumulatively-Stacked Small Molecules/Fluoropolymer/Copper-Oxide Nanoparticles Heterostructure. *Adv. Electron. Mater.* **2022**, *8*, 2200752. [[CrossRef](#)]
51. Kuribara, K.; Wang, H.; Uchiyama, N.; Fukuda, K.; Yokota, T.; Zschieschang, U.; Jaye, C.; Fischer, D.; Klauk, H.; Yamamoto, T. Organic transistors with high thermal stability for medical applications. *Nat. Commun.* **2012**, *3*, 723. [[CrossRef](#)]
52. Cong, S.; Cao, Y.; Fang, X.; Wang, Y.; Liu, Q.; Gui, H.; Shen, C.; Cao, X.; Kim, E.S.; Zhou, C. Carbon nanotube macroelectronics for active matrix polymer-dispersed liquid crystal displays. *ACS Nano* **2016**, *10*, 10068–10074. [[CrossRef](#)]
53. Ohara, H.; Sasaki, T.; Noda, K.; Ito, S.; Sasaki, M.; Endo, Y.; Yoshitomi, S.; Sakata, J.; Serikawa, T.; Yamazaki, S. 4.0-inch active-matrix organic light-emitting diode display integrated with driver circuits using amorphous In–Ga–Zn-Oxide thin-film transistors with suppressed variation. *Jpn. J. Appl. Phys.* **2010**, *49*, 03CD02. [[CrossRef](#)]
54. Mizukami, M.; Oku, S.; Cho, S.-I.; Tatetsu, M.; Abiko, M.; Mamada, M.; Sakanoue, T.; Suzuri, Y.; Kido, J.; Tokito, S. A solution-processed organic thin-film transistor backplane for flexible multiphoton emission organic light-emitting diode displays. *IEEE Electron Device Lett.* **2015**, *36*, 841–843. [[CrossRef](#)]
55. Zhao, T.-Y.; Zhang, D.-D.; Qu, T.-Y.; Fang, L.-L.; Zhu, Q.-B.; Sun, Y.; Cai, T.-H.; Chen, M.-L.; Wang, B.-W.; Du, J.-H. Flexible 64× 64 pixel AMOLED displays driven by uniform carbon nanotube thin-film transistors. *ACS Appl. Mater. Interfaces* **2019**, *11*, 11699–11705. [[CrossRef](#)] [[PubMed](#)]
56. Lee, D.; Cho, E.-S.; Jeon, Y.; Kwon, S.J. Characterization of the material and electrical properties depending on the Mg: Ag ratio as a cathode for TEOLED. *Mater. Chem. Phys.* **2023**, *303*, 127742. [[CrossRef](#)]
57. Park, J.H.; Shin, Y.J.; Kymissis, I.; Jeon, Y.; Kim, C.-H. Frequency-triggered circuit transition in organic light-emitting diodes probed by impedance spectroscopy. *J. Mater. Chem. C* **2023**, *11*, 9670–9677. [[CrossRef](#)]
58. Hwangbo, S.; Hu, L.; Hoang, A.T.; Choi, J.Y.; Ahn, J.-H. Wafer-scale monolithic integration of full-colour micro-LED display using MoS₂ transistor. *Nat. Nanotechnol.* **2022**, *17*, 500–506. [[CrossRef](#)] [[PubMed](#)]
59. Ma, T.; Chen, J.; Chen, Z.; Liang, L.; Hu, J.; Shen, W.; Li, Z.; Zeng, H. Progress in Color Conversion Technology for Micro-LED. *Adv. Mater. Technol.* **2023**, *8*, 2200632. [[CrossRef](#)]
60. Li, Y.; He, P.; Chen, S.; Lan, L.; Dai, X.; Peng, J. Inkjet-printed oxide thin-film transistors based on nanopore-free aqueous-processed dielectric for active-matrix quantum-dot light-emitting diode displays. *ACS Appl. Mater. Interfaces* **2019**, *11*, 28052–28059. [[CrossRef](#)] [[PubMed](#)]
61. Choi, M.K.; Yang, J.; Kang, K.; Kim, D.C.; Choi, C.; Park, C.; Kim, S.J.; Chae, S.I.; Kim, T.-H.; Kim, J.H. Wearable red–green–blue quantum dot light-emitting diode array using high-resolution intaglio transfer printing. *Nat. Commun.* **2015**, *6*, 7149. [[CrossRef](#)]
62. Peng, B.; Ren, X.; Wang, Z.; Wang, X.; Roberts, R.C.; Chan, P.K. High performance organic transistor active-matrix driver developed on paper substrate. *Sci. Rep.* **2014**, *4*, 6430. [[CrossRef](#)]
63. Um, J.G.; Jeong, D.Y.; Jung, Y.; Moon, J.K.; Jung, Y.H.; Kim, S.; Kim, S.H.; Lee, J.S.; Jang, J. Active-Matrix GaN μ -LED Display Using Oxide Thin-Film Transistor Backplane and Flip Chip LED Bonding. *Adv. Electron. Mater.* **2019**, *5*, 1800617. [[CrossRef](#)]
64. Choi, M.; Park, Y.J.; Sharma, B.K.; Bae, S.-R.; Kim, S.Y.; Ahn, J.-H. Flexible active-matrix organic light-emitting diode display enabled by MoS₂ thin-film transistor. *Sci. Adv.* **2018**, *4*, eaas8721. [[CrossRef](#)]
65. Baek, G.W.; Seo, S.G.; Hahm, D.; Kim, Y.J.; Kim, K.; Lee, T.; Kim, J.; Bae, W.K.; Jin, S.H.; Kwak, J. Optimum Design Configuration of Thin-Film Transistors And Quantum-Dot Light-Emitting Diodes for Active-Matrix Displays. *Adv. Mater.* **2023**, *35*, 2304717. [[CrossRef](#)]
66. Kaminishi, D.; Ozaki, H.; Ohno, Y.; Maehashi, K.; Inoue, K.; Matsumoto, K.; Seri, Y.; Masuda, A.; Matsumura, H. Air-stable n-type carbon nanotube field-effect transistors with Si₃N₄ passivation films fabricated by catalytic chemical vapor deposition. *Appl. Phys. Lett.* **2005**, *86*, 113115. [[CrossRef](#)]
67. Filiatrault, H.L.; Porteous, G.C.; Carmichael, R.S.; Davidson, G.J.; Carmichael, T.B. Stretchable light-emitting electrochemical cells using an elastomeric emissive material. *Adv. Mater.* **2012**, *24*, 2673–2678. [[CrossRef](#)] [[PubMed](#)]
68. Liang, J.; Li, L.; Niu, X.; Yu, Z.; Pei, Q. Elastomeric polymer light-emitting devices and displays. *Nat. Photonics* **2013**, *7*, 817–824. [[CrossRef](#)]
69. Liang, J.; Chu, M.; Zhou, Z.; Yan, Y.; Zhao, Y.S. Optically pumped lasing in microscale light-emitting electrochemical cell arrays for multicolor displays. *Nano Lett.* **2020**, *20*, 7116–7122. [[CrossRef](#)] [[PubMed](#)]
70. Meier, S.B.; Tordera, D.; Pertegas, A.; Roldan-Carmona, C.; Orti, E.; Bolink, H.J. Light-emitting electrochemical cells: Recent progress and future prospects. *Mater. Today* **2014**, *17*, 217–223. [[CrossRef](#)]
71. Liu, J.; Wang, J.; Zhang, Z.; Molina-Lopez, F.; Wang, G.-J.N.; Schroeder, B.C.; Yan, X.; Zeng, Y.; Zhao, O.; Tran, H. Fully stretchable active-matrix organic light-emitting electrochemical cell array. *Nat. Commun.* **2020**, *11*, 3362. [[CrossRef](#)]
72. Hong, S.; Choi, S.H.; Park, J.; Yoo, H.; Oh, J.Y.; Hwang, E.; Yoon, D.H.; Kim, S. Sensory adaptation and neuromorphic phototransistors based on CsPb(Br_{1-x}I_x)₃ perovskite and MoS₂ hybrid structure. *ACS Nano* **2020**, *14*, 9796–9806. [[CrossRef](#)]
73. Li, P.; Shan, X.; Lin, Y.; Meng, X.; Ma, J.; Wang, Z.; Zhao, X.; Li, B.; Liu, W.; Xu, H. Tin Doping Induced High-Performance Solution-Processed Ga₂O₃ Photosensor toward Neuromorphic Visual System. *Adv. Funct. Mater.* **2023**, *33*, 2303584. [[CrossRef](#)]
74. Hong, S.; Baek, S.; Can, T.T.T.; Choi, W.S.; Kim, S. Fabrication of Highly Photosensitive MoS₂ Photodetector Films Using Rapid Electrohydrodynamic-Jet Printing Process. *Adv. Electron. Mater.* **2022**, *8*, 2101063. [[CrossRef](#)]
75. Li, M.; Zheng, J.; Wang, X.; Yu, R.; Wang, Y.; Qiu, Y.; Cheng, X.; Wang, G.; Chen, G.; Xie, K. Light-responsive self-strained organic semiconductor for large flexible OFET sensing array. *Nat. Commun.* **2022**, *13*, 4912. [[CrossRef](#)] [[PubMed](#)]

76. Tang, Y.; Zhao, Y.; Liu, H. Room-temperature semiconductor gas sensors: Challenges and opportunities. *ACS Sens.* **2022**, *7*, 3582–3597. [[CrossRef](#)]
77. Shaji, M.; Saji, K.; Jayaraj, M. Low temperature operated ZTO thin film transistor based gas sensor for selective detection of H₂S. *Mater. Sci. Semicond. Process.* **2022**, *150*, 106927. [[CrossRef](#)]
78. Kwon, H.; Yoo, H.; Nakano, M.; Takimiya, K.; Kim, J.-J.; Kim, J.K. Gate-tunable gas sensing behaviors in air-stable ambipolar organic thin-film transistors. *RSC Adv.* **2020**, *10*, 1910–1916. [[CrossRef](#)]
79. Someya, T.; Sekitani, T.; Iba, S.; Kato, Y.; Kawaguchi, H.; Sakurai, T. A large-area, flexible pressure sensor matrix with organic field-effect transistors for artificial skin applications. *Proc. Natl. Acad. Sci. USA* **2004**, *101*, 9966–9970. [[CrossRef](#)] [[PubMed](#)]
80. Hassinen, T.; Eiroma, K.; Mäkelä, T.; Ermolov, V. Printed pressure sensor matrix with organic field-effect transistors. *Sens. Actuators A Phys.* **2015**, *236*, 343–348. [[CrossRef](#)]
81. Trung, T.Q.; Tien, N.T.; Kim, D.; Jang, M.; Yoon, O.J.; Lee, N.E. A flexible reduced graphene oxide field-effect transistor for ultrasensitive strain sensing. *Adv. Funct. Mater.* **2014**, *24*, 117–124. [[CrossRef](#)]
82. Dubey, P.K.; Yogeswaran, N.; Liu, F.; Vilouras, A.; Kaushik, B.K.; Dahiya, R. Monolayer MoSe₂-based tunneling field effect transistor for ultrasensitive strain sensing. *IEEE Trans. Electron Devices* **2020**, *67*, 2140–2146. [[CrossRef](#)]
83. Wang, H.; Tong, Y.; Zhao, X.; Tang, Q.; Liu, Y. Flexible, high-sensitive, and wearable strain sensor based on organic crystal for human motion detection. *Org. Electron.* **2018**, *61*, 304–311. [[CrossRef](#)]
84. Zhu, C.; Chortos, A.; Wang, Y.; Pfattner, R.; Lei, T.; Hinckley, A.C.; Pochorovski, I.; Yan, X.; To, J.W.-F.; Oh, J.Y. Stretchable temperature-sensing circuits with strain suppression based on carbon nanotube transistors. *Nat. Electron.* **2018**, *1*, 183–190. [[CrossRef](#)]
85. Seo, H.; Aihara, S.; Watabe, T.; Ohtake, H.; Sakai, T.; Kubota, M.; Egami, N.; Hiramatsu, T.; Matsuda, T.; Furuta, M.; et al. A 128 × 96 Pixel Stack-Type Color Image Sensor: Stack of Individual Blue-, Green-, and Red-Sensitive Organic Photoconductive Films Integrated with a ZnO Thin Film Transistor Readout Circuit. *Jpn. J. Appl. Phys.* **2011**, *50*, 024103. [[CrossRef](#)]
86. Park, T.; Hur, J. Self-powered low-cost UVC sensor based on organic-inorganic heterojunction for partial discharge detection. *Small* **2021**, *17*, 2100695. [[CrossRef](#)]
87. Zhang, Z.-X.; Li, C.; Lu, Y.; Tong, X.-W.; Liang, F.-X.; Zhao, X.-Y.; Wu, D.; Xie, C.; Luo, L.-B. Sensitive deep ultraviolet photodetector and image sensor composed of inorganic lead-free Cs₃Cu₂I₅ perovskite with wide bandgap. *J. Phys. Chem. Lett.* **2019**, *10*, 5343–5350. [[CrossRef](#)] [[PubMed](#)]
88. Zhang, Y.; Peng, M.; Liu, Y.; Zhang, T.; Zhu, Q.; Lei, H.; Liu, S.; Tao, Y.; Li, L.; Wen, Z. Flexible self-powered real-time ultraviolet photodetector by coupling triboelectric and photoelectric effects. *ACS Appl. Mater. Interfaces* **2020**, *12*, 19384–19392. [[CrossRef](#)]
89. Li, D.; Jia, Z.; Tang, Y.; Song, C.; Liang, K.; Ren, H.; Li, F.; Chen, Y.; Wang, Y.; Lu, X.; et al. Inorganic–Organic Hybrid Phototransistor Array with Enhanced Photogating Effect for Dynamic Near-Infrared Light Sensing and Image Preprocessing. *Nano Lett.* **2022**, *22*, 5434–5442. [[CrossRef](#)]
90. Li, D.; Du, J.; Tang, Y.; Liang, K.; Wang, Y.; Ren, H.; Wang, R.; Meng, L.; Zhu, B.; Li, Y. Flexible and Air-Stable Near-Infrared Sensors Based on Solution-Processed Inorganic–Organic Hybrid Phototransistors. *Adv. Funct. Mater.* **2021**, *31*, 2105887. [[CrossRef](#)]
91. Takahashi, T.; Yu, Z.; Chen, K.; Kiriya, D.; Wang, C.; Takei, K.; Shiraki, H.; Chen, T.; Ma, B.; Javey, A. Carbon nanotube active-matrix backplanes for mechanically flexible visible light and X-ray imagers. *Nano Lett.* **2013**, *13*, 5425–5430. [[CrossRef](#)]
92. Kim, J.; Jo, C.; Kim, M.G.; Park, G.S.; Marks, T.J.; Facchetti, A.; Park, S.K. Vertically Stacked Full Color Quantum Dots Phototransistor Arrays for High-Resolution and Enhanced Color-Selective Imaging. *Adv. Mater.* **2022**, *34*, 2106215. [[CrossRef](#)] [[PubMed](#)]
93. Ruiz-Preciado, L.A.; Baek, S.; Strobel, N.; Xia, K.; Seiberlich, M.; Park, S.-m.; Lemmer, U.; Jung, S.; Hernandez-Sosa, G. Monolithically printed all-organic flexible photosensor active matrix. *NPJ Flex. Electron.* **2023**, *7*, 6. [[CrossRef](#)]
94. Kim, S.; Park, H.; Choo, S.; Baek, S.; Kwon, Y.; Liu, N.; Yang, J.Y.; Yang, C.-W.; Yoo, G.; Kim, S. Active-matrix monolithic gas sensor array based on MoS₂ thin-film transistors. *Commun. Mater.* **2020**, *1*, 86. [[CrossRef](#)]
95. Shin, S.-H.; Ji, S.; Choi, S.; Pyo, K.-H.; Wan An, B.; Park, J.; Kim, J.; Kim, J.-Y.; Lee, K.-S.; Kwon, S.-Y. Integrated arrays of air-dielectric graphene transistors as transparent active-matrix pressure sensors for wide pressure ranges. *Nat. Commun.* **2017**, *8*, 14950. [[CrossRef](#)] [[PubMed](#)]
96. Jang, J.; Kim, H.; Ji, S.; Kim, H.J.; Kang, M.S.; Kim, T.S.; Won, J.-e.; Lee, J.-H.; Cheon, J.; Kang, K. Mechanoluminescent, air-dielectric MoS₂ transistors as active-matrix pressure sensors for wide detection ranges from footsteps to cellular motions. *Nano Lett.* **2019**, *20*, 66–74. [[CrossRef](#)] [[PubMed](#)]
97. Zhao, Z.; Tang, J.; Yuan, J.; Li, Y.; Dai, Y.; Yao, J.; Zhang, Q.; Ding, S.; Li, T.; Zhang, R. Large-scale integrated flexible tactile sensor Array for sensitive smart robotic touch. *ACS Nano* **2022**, *16*, 16784–16795. [[CrossRef](#)] [[PubMed](#)]
98. Karner-Petritz, E.; Petritz, A.; Uemura, T.; Namba, N.; Araki, T.; Sekitani, T.; Stadlober, B. Ultraflexible Organic Active Matrix Sensor Sheet for Tactile and Biosignal Monitoring. *Adv. Electron. Mater.* **2023**, *9*, 2201333. [[CrossRef](#)]
99. Sun, Q.; Seung, W.; Kim, B.J.; Seo, S.; Kim, S.W.; Cho, J.H. Active matrix electronic skin strain sensor based on piezopotential-powered graphene transistors. *Adv. Mater.* **2015**, *27*, 3411–3417. [[CrossRef](#)]
100. Oh, J.Y.; Son, D.; Katsumata, T.; Lee, Y.; Kim, Y.; Lopez, J.; Wu, H.-C.; Kang, J.; Park, J.; Gu, X. Stretchable self-healable semiconducting polymer film for active-matrix strain-sensing array. *Sci. Adv.* **2019**, *5*, eaav3097. [[CrossRef](#)]
101. Li, C.-H.; Wang, C.; Keplinger, C.; Zuo, J.-L.; Jin, L.; Sun, Y.; Zheng, P.; Cao, Y.; Lissel, F.; Linder, C. A highly stretchable autonomous self-healing elastomer. *Nat. Chem.* **2016**, *8*, 618–624. [[CrossRef](#)]

102. Li, M.; Chen, S.; Fan, B.; Wu, B.; Guo, X. Printed flexible strain sensor array for bendable interactive surface. *Adv. Funct. Mater.* **2020**, *30*, 2003214. [[CrossRef](#)]
103. Zhao, J.; Wei, Z.; Li, Z.; Yu, J.; Tang, J.; Zhang, G.; Wang, Z. Skin-Inspired High-Performance Active-matrix Circuitry for Multimodal User-Interaction. *Adv. Funct. Mater.* **2021**, *31*, 2105480. [[CrossRef](#)]
104. Hong, S.Y.; Lee, Y.H.; Park, H.; Jin, S.W.; Jeong, Y.R.; Yun, J.; You, I.; Zi, G.; Ha, J.S. Stretchable active matrix temperature sensor array of polyaniline nanofibers for electronic skin. *Adv. Mater.* **2016**, *28*, 930–935. [[CrossRef](#)] [[PubMed](#)]
105. Ren, X.; Pei, K.; Peng, B.; Zhang, Z.; Wang, Z.; Wang, X.; Chan, P.K. A low-operating-power and flexible active-matrix organic-transistor temperature-sensor array. *Adv. Mater.* **2016**, *28*, 4832–4838. [[CrossRef](#)] [[PubMed](#)]
106. Kim, J.S.; Jeong, M.W.; Nam, T.U.; Vo, N.T.P.; Jung, K.H.; Lee, T.I.; Oh, J.Y. Intrinsically Stretchable Subthreshold Organic Transistors for Highly Sensitive Low-Power Skin-Like Active-Matrix Temperature Sensors. *Adv. Funct. Mater.* **2023**, *34*, 2305252. [[CrossRef](#)]

Disclaimer/Publisher’s Note: The statements, opinions and data contained in all publications are solely those of the individual author(s) and contributor(s) and not of MDPI and/or the editor(s). MDPI and/or the editor(s) disclaim responsibility for any injury to people or property resulting from any ideas, methods, instructions or products referred to in the content.